A&A 407, 845–854 (2003)
DOI: 10.1051/0004-6361:20030991

Astronomy & Astrophysics

Stacking clusters in the ROSAT All-Sky Survey

M. Bartelmann and S. D. M. White

Max-Planck-Institut für Astrophysik, PO Box 1317, 85741 Garching, Germany

Received 2 October 2002 / Accepted 25 June 2003

Abstract. Ongoing and planned wide-area surveys at optical and infrared wavelengths should detect a few times 10^5 galaxy clusters, roughly 10% of which are expected to be at redshifts $\gtrsim$0.8. We investigate what can be learned about the X-ray emission of these clusters from the ROSAT All-Sky Survey. While individual clusters at redshifts $\gtrsim$0.5 contribute at most a few photons to the survey, a significant measurement of the mean flux of cluster subsamples can be obtained by stacking cluster fields. We show that the mean X-ray luminosity of clusters with mass $M \gtrsim 2 \times 10^{14}\,h^{-1}M_\odot$ selected from the Sloan Digital Sky Survey should be measurable out to redshift unity with signal-to-noise $\gtrsim$10, even if clusters are binned with $\Delta z = 0.1$ and $\Delta \ln M \sim 0.3$. For such bins, a suitably chosen hardness ratio allows the mean temperature of clusters to be determined out to $z \sim 0.7$ with a relative accuracy of $\Delta T/T \lesssim 0.15$ for $M > 10^{14}\,h^{-1}M_\odot$.

Key words. surveys – galaxies: clusters: general – X-rays: galaxies

1. Introduction

With moderately deep, wide-area imaging surveys in the optical or near infrared it is now possible to detect large samples of galaxy clusters. Dalcanton (1996) proposed that clusters could be detected as surface brightness enhancements even when all but a few of their galaxies are too faint to be detected individually. Her suggested procedure consists of identifying and removing stars and galaxies from carefully flat-fielded images, smoothing the residual with a kernel matched to the core size of clusters, and searching for significant peaks in the resulting smoothed map. Gonzalez et al. (2001) successfully constructed the Las Campanas Distant Cluster Survey (LCDCS) by applying this technique to drift-scan data taken with the Las Campanas Great Circle Camera (Zaritsky et al. 1996). They mapped well over 100 square degrees and constructed a catalog of 1073 groups and clusters. The estimated redshift limits of the catalog range from ∼0.3 for groups to ∼0.9 for massive galaxy clusters.

The high intrinsic uniformity of drift-scan surveys like the LCDCS makes them ideal for applying Dalcanton's cluster-detection technique. In a theoretical study, Bartelmann & White (2002) showed that massive galaxy clusters should be detectable in the Sloan Digital Sky Survey (SDSS) out to redshifts of ∼1.2 if data in the r', i' and z' bands are summed. For the final projected SDSS survey area of 10^4 square degrees, $\gtrsim 10^5$ galaxy clusters should be detectable at the 5-σ level, and ∼10% of those are expected to be at redshifts $\gtrsim$0.8.

Until very recently, relatively little was known about the X-ray emission of clusters at redshifts beyond ∼0.5 despite numerous cluster surveys based on X-ray data. The main reason for this is the steep decrease with redshift of the observed X-ray flux, which implies that at $z > 0.5$ individual massive clusters produce at most a few photons in surveys like the ROSAT All-Sky Survey (RASS; Snowden & Schmitt 1990). In the past couple of years, pointed observations with Chandra and XMM have significantly improved our knowledge of clusters at moderate to high redshift. An evolution of the X-ray luminosity function between $z \lesssim 0.8$ and the present epoch has now been clearly established (see Henry 2003 for a review). The situation is less clear for the luminosity-temperature relation. For example, Hashimoto et al. (2002) find the cluster RX J1053.7 + 5735 at redshift $z = 1.26$ to be compatible with little or no evolution in the $L_X - T$ relation, while Vikhlinin et al. (2002) find that correlations between cluster temperature, X-ray luminosity, and gas mass evolve significantly between redshift $z \approx 0.5$ and today. On the whole, modest evolution of the cluster population since redshift unity, and a substantial impact of non-gravitational heating on the thermal history of the intracluster gas seem to be firmly established (e.g. Rosati et al. 2002). Testing theoretical models for cluster evolution now requires large cluster samples out to moderate and high redshift.

The upcoming availability of large cluster surveys in wavebands other than the X-ray regime allows a reversal of the traditional X-ray survey strategy. Rather than identifying clusters in the X-ray data, it becomes possible to stack X-ray survey data for a large number of fields where clusters are already known from other surveys. The low background count rate at X-ray wavelengths makes this an efficient technique for detecting the summed emission from a large stack of clusters.

Send offprint requests to: M.Bartelmann,
e-mail: msb@mpa-garching.mpg.de

Such a study would be useful for many purposes. Predictions for the number of clusters detectable in the optical to high redshift depend on the cluster mass function and its cosmic evolution, as well as on the mass-to-light ratio of the clusters and its scatter. Expectations for the average X-ray emission of optically selected clusters require a model for the thermal evolution of the intracluster gas, and assumptions on its physical state, e.g. virial and hydrostatic equilibrium in the dark-matter gravitational potential well. If a large dataset on the average X-ray emission of optically selected galaxy clusters to high redshifts can be compiled, theoretically motivated assumptions on the mass, thermal, and optical evolution of the cluster population can be tested.

In this paper we investigate the prospects for using the RASS to detect X-rays from suitable samples of clusters identified in the SDSS data. In Sect. 2 we describe our model for the cluster population. This is based closely on the properties of nearby clusters and specifies the cluster distribution in mass, redshift, optical luminosity, X-ray temperature and luminosity. In Sect. 3 we convert cluster X-ray luminosities to count distributions expected in the ROSAT All-Sky Survey. Based on these, we calculate in Sect. 4 the expected signal-to-noise both for the detection of mean cluster emission and for estimates of mean cluster temperature. Section 6 summarises and discusses our conclusions.

2. Model specifications

2.1. Cosmology

Much evidence suggests that the universe is spatially flat with low nonrelativistic matter density Ω_0. Baryons make up only a small fraction of this matter; the rest is dark, presumably consisting of some massive, weakly interacting particle. A cosmological constant Ω_Λ or an equivalent "quintessence" field contributes the remaining energy density. For definiteness, we assume $\Omega_0 = 0.3$, $\Omega_\Lambda = 0.7$ and $h = 0.7$

We assume structure to form from an initially Gaussian density fluctuation field δ with statistical properties specified by its linear power spectrum, for which we adopt the CDM form given by Bardeen et al. (1986) with primordial spectral index $n = 1$. The only remaining free parameter is then the normalisation of the initial fluctuation field which we take as $\sigma_8 = 0.9$. This value was originally estimated based on the observed local abundance of galaxy clusters (White et al. 1993; Eke 1996; Viana & Liddle 1996; Pierpaoli et al. 2001; Evrard et al. 2002) but some recent analyses favour smaller values (Reiprich & Böhringer 2002; Viana et al. 2002; Lahav et al. 2002). We will show results for $\sigma_8 = 0.9 \pm 0.1$.

2.2. Cluster population

Haloes form from Gaussian primordial density fluctuations through gravitational collapse. Press & Schechter (1974) first derived an approximate formula for the mass distribution of haloes as a function of redshift z. This has recently been modified by Sheth et al. (2001) and Sheth & Tormen (2002) based on an ellipsoidal rather than a spherical model for collapse. They give the differential comoving number density of haloes as

$$n(M,z)\,\mathrm{d}M = A\sqrt{\frac{2}{\pi}}\left(1+\frac{1}{\nu^{2q}}\right)\frac{\bar{\rho}}{M}\frac{\mathrm{d}\nu}{\mathrm{d}M}\exp\left(-\frac{\nu^2}{2}\right)\mathrm{d}M, \qquad (1)$$

where $\nu = \sqrt{a}\delta_\mathrm{c}\sigma^{-1}(M,z)$ defines the linear amplitude required for collapse of a density fluctuation and $\bar{\rho}$ is the mean cosmic density today. $\sigma(M,z)$ in this definition is equal to $\sigma_0(M)D_+(z)$, where $\sigma_0(M)$ is the present rms fluctuation in the dark matter density contrast within spheres containing the mean mass M, and $D_+(z)$ (with $D_+(0) = 1$) is the growth factor for the linear growing mode (cf. Carroll et al. 1992). The linear density contrast required for collapse δ_c depends weakly on cosmology; for the ΛCDM model we have chosen $\delta_\mathrm{c} = 1.673$ (e.g. Łokas & Hoffman 2001). The parameters A, a and q are constants; the original Press-Schechter formula is obtained from (1) by putting $A = 0.5$, $a = 1$ and $q = 0$. This mass function, with $A = 0.322$, $a = 0.707$ and $q = 0.3$, has been shown to fit high resolution numerical simulations of structure growth in a wide range of cosmologies, provided the halo mass is defined at fixed density contrast relative to the cosmic mean density (Jenkins et al. 2001).

Next, we need to know the X-ray luminosity of a cluster of mass M. We adopt the observed relation between cluster temperature T and bolometric X-ray luminosity L_X

$$L_\mathrm{X} = 10^{44}\,h_{50}^{-2}\mathrm{erg\,s^{-1}}\left(\frac{kT}{1.66\,\mathrm{keV}}\right)^{2.331}, \qquad (2)$$

as derived by Allen & Fabian (1998). Observations suggest that there is little evolution in the $L_\mathrm{X} - T$ relation out to redshifts $z \sim 0.4$ (e.g. Mushotzky & Scharf 1997; Allen & Fabian 1998; Reichart et al. 1999) and even well beyond (Hashimoto et al. 2002). Lacking any reliable information about evolution to higher redshifts, we assume (2) to hold at all redshifts. This, of course, is a major uncertainty of our study.

According to the virial theorem, a halo of mass M in equilibrium at redshift z with a structure similar to observed clusters should have a mean temperature given by

$$kT = 4.88\,\mathrm{keV}\left[\frac{M\,h(z)}{10^{15}M_\odot}\right]^{2/3}, \qquad (3)$$

where $h(z)$ is the Hubble constant at redshift z in units of $100\,\mathrm{km\,s^{-1}\,Mpc^{-1}}$ and, in contrast to Eq. (1), M is here defined as the mass interior to a sphere with mean overdensity 200 times the *critical* value at redshift z. Recall that we assume $h(0) = 0.7$ throughout our analysis. The constant in this relation is taken from the cluster simulations of Mathiesen & Evrard (1901; their Table 1) and is appropriate for specifying the temperature of the best fit single temperature model for the X-ray spectrum over the mass and redshift ranges of interest. When necessary, we use an NFW model of concentration parameter 5 to convert between cluster masses defined at different overdensities.

Both the luminosity-temperature relation (2) and the mass-temperature relation (3) have been the subject of much recent debate. Allen & Fabian (1998) derived (2) from clusters whose cooling-flow regions were excised. Among others,

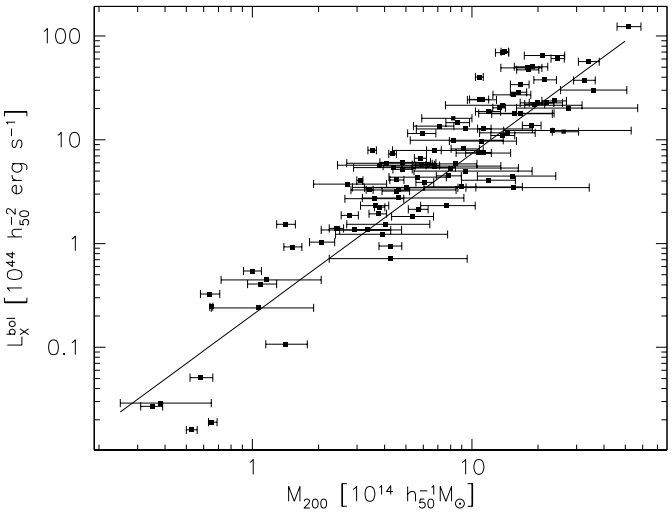

Fig. 1. Comparison between the luminosity-mass relation used here (solid line) and the data compiled by Reiprich & Böhringer (2002; data points). Within the error bars, the agreement is very good.

Ikebe et al. (2002) find a somewhat steeper $L_X - T$ relation. Horner et al. (1999) find that mass estimates from X-ray observations fall below the $M - T$ relation (3) and scale more steeply with temperature. In a detailed study of A 3571 with BeppoSAX, Nevalainen et al. (2001) find a significantly lower X-ray mass than expected from the measured temperature and relation (3). For the purposes of our paper, however, we need Eqs. (2) and (3) for predicting the X-ray luminosity of a cluster with mass M, hence the cluster temperature is an intermediate variable without further significance for our later predictions. We only have to demonstrate that the mass-luminosity relation obtained from (2) and (3) agrees with observational results.

Probably the best current observational sample has been compiled by Reiprich & Böhringer (2002). A fit to their complete sample of 106 bright ROSAT-selected X-ray clusters with masses determined mainly from ASCA temperature observations yields

$$\frac{L_{X,bol}}{10^{44}\,h_{50}^{-2}\,\mathrm{erg\,s^{-1}}} = 0.28\,h_{50}^{-2}\,\mathrm{erg\,s^{-1}}\left(\frac{M_{200}}{10^{14}\,h_{50}^{-1}\,M_\odot}\right)^{1.56}, \qquad (4)$$

while inserting (3) into (2) implies

$$\frac{L_{X,bol}}{10^{44}\,h_{50}^{-2}\,\mathrm{erg\,s^{-1}}} = 0.21\,h_{50}^{-2}\,\mathrm{erg\,s^{-1}}\left(\frac{M_{200}}{10^{14}\,h_{50}^{-1}\,M_\odot}\right)^{1.554}. \qquad (5)$$

To within the remaining uncertainties, these two relations are in very good agreement, showing that the luminosity-mass relation underlying our further calculations is well justified, as Fig. 1 illustrates.

The agreement between the observed and theoretically expected $L_X - M_{200}$ relations (4) and (5) appears surprising in view of the doubts raised against the ingredient relations (2) and (3). It may be caused by both the $L_X - T$ and $M - T$ relations being somewhat flatter than observed, leading to a cancellation of their mutual deviations when combined into a single $L_X - M$ relation.

2.3. X-ray emission

Clusters emit X-rays through thermal *bremsstrahlung*, which we assume to be well-described by a Raymond-Smith plasma model (Raymond & Smith 1977). Apart from cluster temperature and redshift, the model has two free parameters, the metal abundance and an overall normalisation corresponding to the total X-ray luminosity. We fix the metal abundance to $Z = 0.3\,Z_\odot$ at all z in agreement with the observed abundances of local clusters (e.g. Fukazawa et al. 1998). The results of Schindler (1999) suggest little evolution towards higher redshift and the final count rates we derive depend only very weakly on metallicity. Thus neglecting any dependence on redshift does not induce significant uncertainty.

Let $F_\nu(T,z)\mathrm{d}\nu$ be the total X-ray luminosity emitted in the spectral interval $[\nu, \nu + \mathrm{d}\nu]$ by a cluster of temperature T at redshift z. If the cluster is observed in an energy band bounded by E_1 and $E_2 > E_1$, only a fraction f of its bolometric flux is included in the bandpass, where

$$f = \int_{E_1(1+z)}^{E_2(1+z)} F_\nu(T,z)\,\mathrm{d}\nu \left[\int_0^\infty F_\nu(T,z)\,\mathrm{d}\nu\right]^{-1}. \qquad (6)$$

Thus the band-limited flux S_X is related to the bolometric X-ray luminosity through

$$S_X = \frac{f\,L_X}{4\pi D_L^2(z)}, \qquad (7)$$

where $D_L(z)$ is the luminosity distance from the observer to redshift z. Note that this flux must still be modified to account for foreground absorption.

We use version 11.1 of the *xspec* software package (Arnaud 1996) to tabulate f for an observing band between 0.5 and 2.4 keV, for cluster temperatures between 0.5 and 12 keV, and for redshifts between 0 and 2. Interpolating within this table and using Eqs. (2), (3) and (7), we can convert cluster masses to cluster temperatures, X-ray luminosities, and finally to unabsorbed fluxes in the observed energy range.

The azimuthally averaged X-ray surface brightness profile $\Sigma(\theta)$ of galaxy clusters is often modelled using the so-called beta profile (Cavaliere & Fusco-Femiano 1978),

$$\Sigma(\theta) = \Sigma_0\left[1 + \left(\frac{\theta}{\theta_c}\right)^2\right]^{-(3\beta-1/2)}, \qquad (8)$$

where θ_c is an angular core radius, and the amplitude Σ_0 is chosen to produce the required X-ray flux S_X. Based on observation, we choose $\beta = 2/3$ (e.g. Mohr et al. 1999). For the linear core radius r_c, we adopt the relation

$$r_c = 125\,\mathrm{kpc}\,h^{-1}\left(\frac{L_X}{5\times10^{44}\,\mathrm{erg\,s^{-1}}}\right)^{0.2}, \qquad (9)$$

where L_X is the X-ray luminosity between 0.5 and 2.4 keV. This relation is a fair representation of at least some clusters with luminosities within $10^{43-45}\,\mathrm{erg\,s^{-1}}$ (Jones et al. 1998). Following Vikhlinin et al. (1998), we assume that (9) does not evolve with redshift. The angular core radius is then $\theta_c = r_c\,D^{-1}(z)$, where $D(z)$ is the angular-diameter distance. In fact, Eq. (8) is a poor fit to the profiles of many clusters, particularly those

with strong apparent cooling flows. This is not, however, of any great consequence for our modelling since the RASS does not, in any case, resolve the inner regions of most clusters.

Having fixed β, S_X and the angular core radius θ_c, the beta profile is normalised by

$$\Sigma_0 = \frac{S_X}{2\pi\theta_c^2}. \tag{10}$$

3. Halo detection

3.1. Point-spread function

The point-spread function $f(\theta, E, \phi)$ of the ROSAT-PSPC had three components, a Gaussian kernel, Lorentzian wings, and a component which falls off exponentially with angular separation θ from the centre of the image (Hasinger et al. 1995). The parameters for these components generally depend not only on photon energy E, but also on ϕ, the off-axis angle of the source.

The width of the PSPC point-spread function can be characterised by the effective solid angle $\delta\Omega(E, \phi)$ covered,

$$\delta\Omega(E, \phi) = 2\pi \int_0^\infty \theta \mathrm{d}\theta\, f(\theta, E, \phi)\,, \tag{11}$$

and we can define an effective radius $\theta_{\mathrm{eff}}(E, \phi)$ by

$$\theta_{\mathrm{eff}}(E, \phi) = \left(\frac{\delta\Omega(E, \phi)}{\pi}\right)^{1/2}. \tag{12}$$

The effective radii for six different off-axis angles between 10′ and 60′ are shown as functions of photon energy in Fig. 2. The dependence of the three components of the PSF on energy and off-axis angle is complicated and determined by several competing contributions. While some terms sharpen the PSF as the photon energy increases, others broaden it, and their relative balance depends on the off-axis angle.

The field-of-view of the PSPC was large, with a radius of approximately 60′. Since a given point on the sky was scanned at many different off-axis angles during the All-Sky Survey, the appropriate point-spread function for the ROSAT All-Sky Survey at a given photon energy is an area-weighted average of $f(\theta, E, \phi)$ over the field-of-view,

$$\bar{f}(\theta, E) = \frac{2}{(60')^2} \int_0^{60'} \phi \mathrm{d}\phi\, f(\theta, E, \phi). \tag{13}$$

Figure 3 shows the result for four different photon energies between 0.5 and 2.0 keV.

Figure 3 shows that the point-spread function, averaged over off-axis angles, falls to ∼10% of its peak value within 2–3 arcmin with little dependence on photon energy. Figure 2 confirms this weak dependence on photon energy, and illustrates the strong dependence of effective PSF radius on off-axis angle. While θ_{eff} is below 0.5′ for nearly on-axis photons, it increases above 1′ for photons coming from the edge of the field-of-view.

The effective radius of the averaged point-spread function $\bar{f}(\theta, E)$ can finally be averaged over photon energies to obtain an average effective radius valid for the hard band of the All-Sky Survey. Performing this average and weighting the photon energies with the effective detector area as a function of E, we find $\bar{\theta}_{\mathrm{eff}} = 2.1'$.

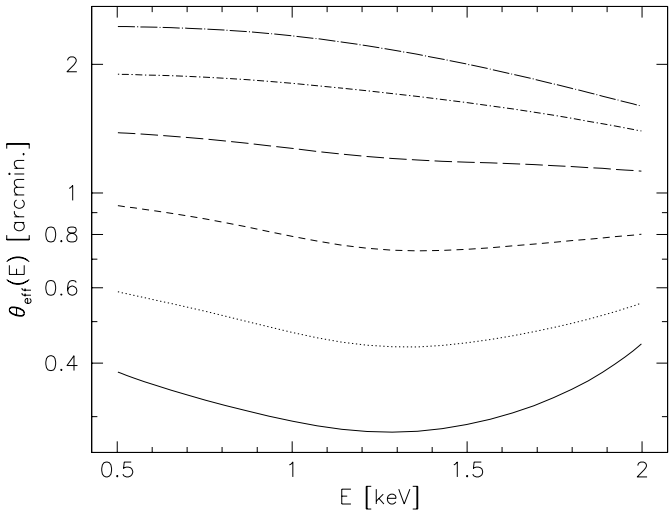

Fig. 2. Effective radii of the PSPC point-spread function as functions of photon energy, for off-axis angles between 10′ and 60′ (from bottom to top).

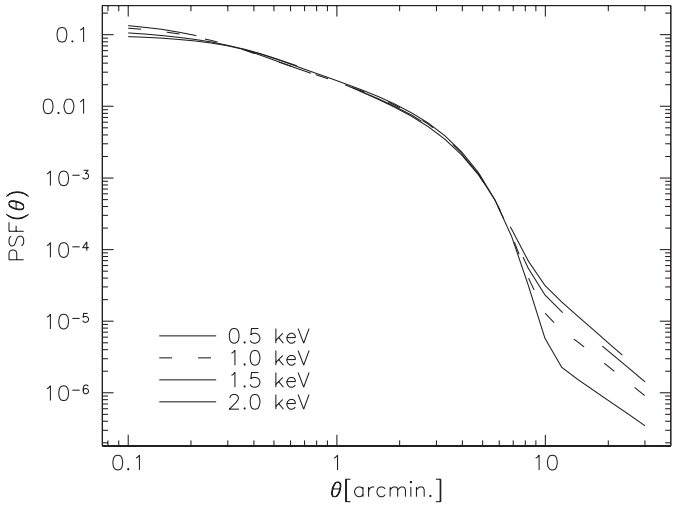

Fig. 3. The ROSAT-PSPC point-spread function, averaged over off-axis angles within the PSPC field-of-view. The different curves show the point-spread function for four different photon energies, as indicated.

3.2. Converting fluxes to count rates

We now need to estimate the signal expected in the All-Sky Survey from a cluster with unabsorbed flux S_X and temperature T at redshift z. To do this, we first modify the fluxes S_X calculated using Eq. (7) to allow for absorption by foreground neutral hydrogen. We assume a constant hydrogen column of $4 \times 10^{20}\,\mathrm{cm}^{-2}$, which is typical for the high galactic latitudes covered by the SDSS (e.g. Dickey & Lockman 1990). We convert the absorbed fluxes to PSPC count rates, using the *fakeit* task of the *xspec* package with the PSPC response matrix[1].

In practice, we compute a two-dimensional table containing PSPC count rates in the energy range between 0.5 and 2 keV for *absorbed* Raymond-Smith spectra of a fixed *unabsorbed*

[1] Electronically provided at
ftp://ftp.xray.mpe.mpg.de/rosat/calibration/data

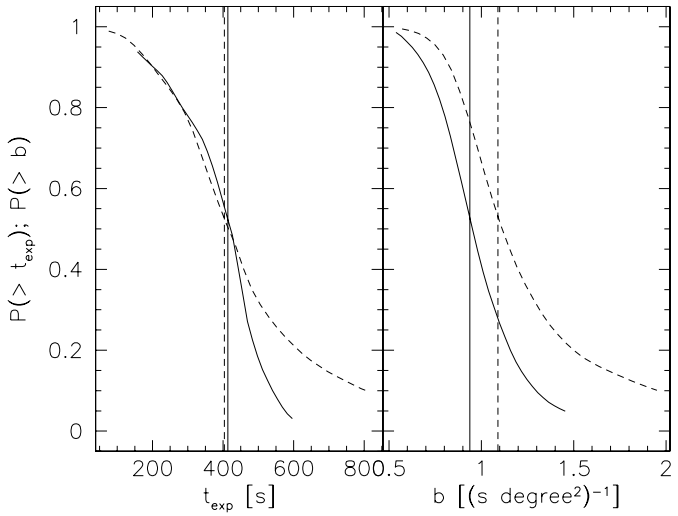

Fig. 4. Cumulative distributions of exposure-time (*left panel*) and background count-rate (*right panel*) in the ROSAT All-Sky Survey. The dashed curves refer to the complete survey, the solid curves to the SDSS area only. The vertical lines mark the medians.

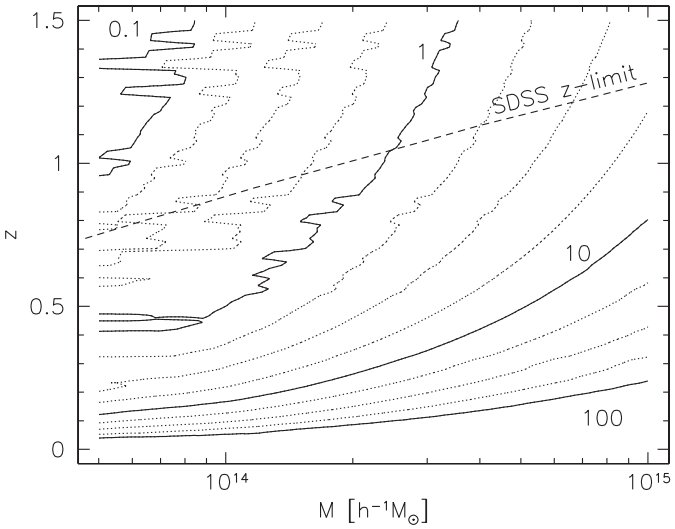

Fig. 5. Contours in the mass-redshift plane showing the counts received per cluster within the effective radius of the PSPC point-spread function. The contours are logarithmically spaced at 0.25 dex between 0.1 (upper solid contour) and 100 counts (lower solid contour). The dashed curve marks the expected upper redshift limit for 5-σ cluster detection in the combined r', i' and z' bands of the SDSS. The contours for low-mass clusters appear jagged because their X-ray spectra have strong features due to heavy elements which move relative to the observed energy band.

flux normalisation and for cluster temperatures between 0.5 and 12 keV and redshifts between 0 and 2. Fluxes determined from (7) can then be converted to absorbed count rates by interpolating within this table.

3.3. Exposure times; background level

The effective exposure time in the All-Sky Survey varies across the sky because of the ROSAT scanning strategy. It is highest near the ecliptic poles and lowest close to the ecliptic plane (cf. Snowden et al. 1995). Maps for the exposure time and the background count rates were downloaded from the ROSAT All-Sky Survey web page[2]. The left panel in Fig. 4 shows the cumulative exposure-time distribution for the complete All-Sky Survey (dashed curve), and for the area around the Northern Galactic cap covered by the Sloan Digital Sky Survey. The median exposure times are marked by vertical lines.

The effective exposure times on the whole sphere and on the SDSS area are only marginally different. For the SDSS area, we find a median value

$$t_{\rm exp} = 414\,{\rm s}. \tag{14}$$

Similarly, the background level is anisotropic across the sky. The right panel in Fig. 4 shows the cumulative distributions of the background count rate in the All-Sky Survey for the whole sky (dashed line) and for the SDSS area (solid line).

The background count rate within the SDSS area is noticeably lower than on the whole sky; its median value is

$$B = 0.94\,{\rm s}^{-1}\,{\rm deg}^{-2} = 2.61\times10^{-4}\,{\rm s}^{-1}\,{\rm arcmin}^{-2}. \tag{15}$$

4. Results

Figure 5 shows photon-count contours in the plane spanned by cluster mass and redshift. On a grid covering that plane, we compute temperature, luminosity, flux, and count rate as described in the previous section. We then multiply the count rate by the median exposure time in the SDSS area, averaged over photon energies in the 0.5−2.4 keV band.

The contours are logarithmically spaced by 0.25 dex between 0.1 and 100 counts (upper and lower solid curves, respectively). They appear jagged because a substantial fraction of the X-ray flux is contributed by metal lines which move in and out of the observed energy band as the redshift changes. The contours become smooth if the metal abundance is set to zero. From this plot one can see, for example, that the redshift limit below which individual clusters contribute more than ten photons to the All-Sky Survey increases from $z_{\rm max}\sim0.1$ at $M = 10^{14}\,h^{-1}\,M_\odot$ to $z_{\rm max}\sim0.8$ at $M = 10^{15}\,h^{-1}\,M_\odot$. The dashed curve shows the redshift limit for detection of clusters as 5-σ surface brightness enhancements in the combined r', i' and z' data of the SDSS (Bartelmann & White 2002). Clearly the SDSS should produce cluster catalogues which are much deeper at all masses than those that can be made from the RASS.

Figure 5 illustrates that only 0.3 photons per cluster are expected for clusters of $M\sim10^{14}\,h^{-1}\,M_\odot$ at redshift $z\sim0.8$. The number of such clusters expected in the SDSS is so large, however, that it should be possible to determine their mean X-ray properties by stacking data for many fields. This is true even if the mass-redshift plane is divided into relatively narrow bins. We now investigate this in more detail.

Figure 5 agrees very well with the results from the MACS cluster survey (Ebeling et al. 2001). Imposing a lower limit of 17 photons, they find clusters in the All-Sky Survey out to redshifts $z\lesssim0.6$. According to Fig. 5, 17 photons at $z = 0.6$

[2] http://www.xray.mpe.mpg.de/cgi-bin/rosat/rosat-survey/

correspond to a limiting mass of $8\times10^{14}\,h^{-1}\,M_\odot$, in good agreement with the masses expected for the most extreme systems at this redshift.

The background level of the All-Sky Survey is quite low, of order $1\,\mathrm{s}^{-1}\,\mathrm{deg}^{-2}$ which translates to approximately 0.8 total counts per resolution element within the median exposure time of the survey. The background will nevertheless dominate the noise in a stacked image of distant clusters. Let B be the mean surface density of background photons in a single image, and $C(M,z)$ be the expected number of photons from a single cluster of mass M at redshift z. Let $p(\theta)$ be the expected surface density of these cluster photons as a function of angular distance θ from cluster centre. $p(\theta)$ is given by a convolution of the mean cluster surface brightness profile (Eq. (8)) with the point-spread-function of the survey (Fig. 3) and we normalise it so that $\int p(\theta)\,2\pi\theta\,\mathrm{d}\theta = 1$. In practice for distant clusters the *p.s.f.* is much broader than the cluster image so that $p(\theta)$ is proportional to the *p.s.f.* itself.

For a stack of N cluster fields the surface density of the background is NB and the expected surface density profile is $NCp(\theta)$. Assuming Poisson photon statistics, the optimal estimator of the cluster signal is then:

$$\tilde{NC} = \int w(\theta)[O(\theta) - B]2\pi\theta\mathrm{d}\theta\,, \tag{16}$$

where $2\pi O(\theta)\theta\mathrm{d}\theta$ is the observed photon count in an annulus width $\mathrm{d}\theta$, and the filter function w, normalised so that $\int w(\theta)p(\theta)\,2\pi\theta\mathrm{d}\theta = 1$, is given by

$$w(\theta) = \frac{p(\theta)}{p(\theta) + B/C}\left[\int \frac{p^2 2\pi\theta\mathrm{d}\theta}{p + B/C}\right]^{-1}. \tag{17}$$

Clearly the expectation value of the estimator of Eq. (16) is just NC while its variance is

$$\mathrm{Var}(\tilde{NC}) = NC\int w^2(\theta)p(\theta)\,2\pi\theta\mathrm{d}\theta. \tag{18}$$

Thus the expected signal-to-noise for detecting the stacked cluster is

$$\left(\frac{S}{N}\right) = (NC)^{1/2}\left[\int \frac{p^2(\theta)\,2\pi\theta\mathrm{d}\theta}{p(\theta) + B/C}\right]^{1/2}. \tag{19}$$

If clusters are individually well above background ($Cp(\theta) \gg B$ over most of the broadened image) this gives the obvious result, $(S/N) \approx (NC)^{1/2}$ for the stack. When background dominates ($Cp(0) \ll B$) the corresponding result is $(S/N) \approx NC/[NB\int p^2(\theta)\,2\pi\theta\mathrm{d}\theta]^{1/2}$. In both cases the signal-to-noise of the detection grows as $N^{1/2}$ for the stacked image. Figure 6 shows the number of cluster fields required for a 5-σ detection in the stacked image as a function of cluster mass and redshift.

Contours are shown for $N = 1$ (lower solid curve), $N = 10$, and $N = 100$ (upper solid curve). The figure shows that it takes 100 stacked cluster fields to obtain a 5-σ detection of clusters with $M \sim 10^{14}\,h^{-1}\,M_\odot$ at redshift $z \sim 0.4$, but the contours rise steeply enough that with the same number of stacked fields one reaches redshifts above unity for cluster masses $M \gtrsim 3\times10^{14}\,h^{-1}\,M_\odot$. As in Fig. 5, the dashed line shows the upper redshift limit expected for 5-σ cluster detection in the combined r', i' and z' bands of the SDSS.

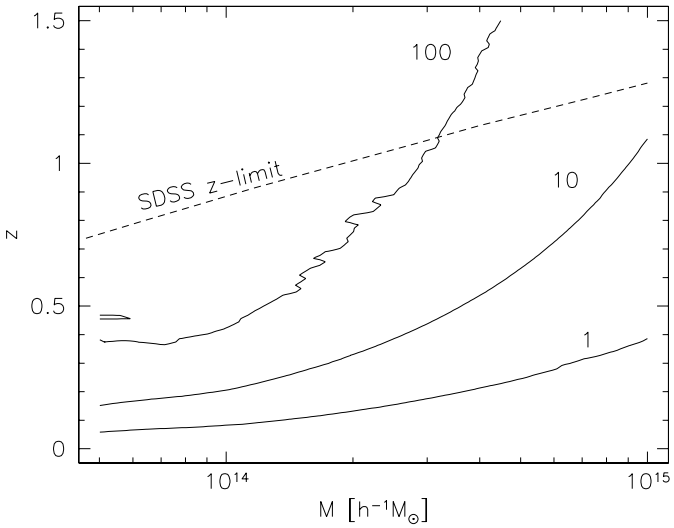

Fig. 6. Number of clusters to be stacked to achieve a 5-σ detection of their total X-ray emission in the ROSAT All-Sky Survey. The contour levels are 1 (lower contour), 10, and 100 (upper contour). The dashed curve marks the expected upper redshift limit for 5-σ cluster detection in the combined r', i' and z' bands of the SDSS.

We now have to compare the number of cluster fields needed to achieve a high signal-to-noise ratio with All-Sky Survey data to the number of clusters we can expect to be available. The idea is to select fields around clusters which are known from other data, and we continue to take the SDSS as an example. We therefore ask how many clusters can be expected in the SDSS data.

To give specific examples, we select two redshift intervals of width $\Delta z = 0.1$ each, one over $0.6 \le z \le 0.7$ and the other over $0.9 \le z \le 1.0$. Our previous work has obtained the expected redshift limit $z_{\mathrm{lim}}(M)$ as a function of cluster mass for detection in SDSS data (Bartelmann & White 2002). For a 5-σ detection in the combined r', i' and z' bands, it is indicated by a dashed line in Figs. 5 and 6. For each redshift interval, we thus know the completeness limit in cluster mass, i.e. the lowest cluster mass M_{lim} above which clusters in that interval are expected to be detectable. For the lower and upper redshift intervals defined above, we obtain $M_{\mathrm{lim}} = 3.9\times10^{13}\,h^{-1}M_\odot$ and $M_{\mathrm{lim}} = 2.0\times10^{14}\,h^{-1}M_\odot$ respectively. For each interval we then define a series of mass bins between M_{lim} and $10^{15}\,h^{-1}M_\odot$ such that $\Delta\ln M \sim 0.3$.

The number of clusters in the redshift interval $[z_i, z_i + \Delta z]$ per mass bin $[M_j, M_{j+1}]$ is obtained through an integral of the mass function (1) multiplied by the comoving cosmic volume,

$$\Delta N_{ij} = \int_{z_i}^{z_i+\Delta z}\mathrm{d}z\int_{M_j}^{M_{j+1}}\mathrm{d}M\,n(M,z)\left|\frac{\mathrm{d}V}{\mathrm{d}z}\right|(1+z)^3. \tag{20}$$

The volume per unit redshift is

$$\left|\frac{\mathrm{d}V}{\mathrm{d}z}\right| = \pi D^2(z)\left|\frac{\mathrm{d}D_{\mathrm{prop}}}{\mathrm{d}z}\right|, \tag{21}$$

where D is the angular diameter distance and D_{prop} the proper distance. The factor π instead of 4π accounts for the fact that the

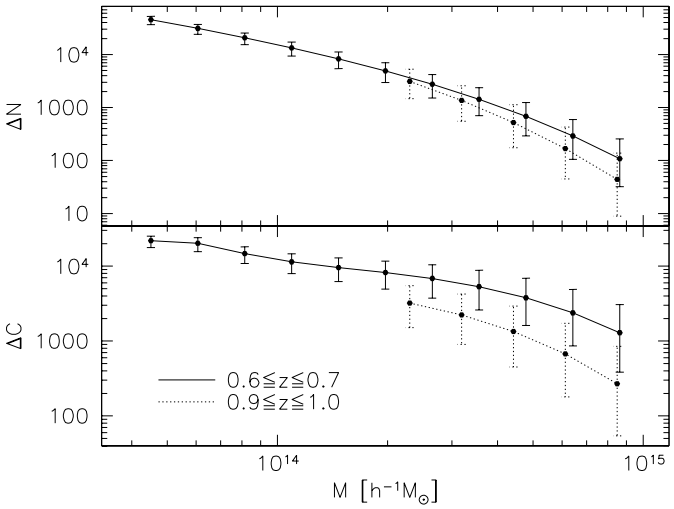

Fig. 7. Number of clusters ΔN (upper panel) and total cluster counts ΔC (lower panel) in the two redshift intervals $0.6 \le z \le 0.7$ (solid curve) and $0.9 \le z \le 1.0$ (dotted curve) in mass bins of logarithmic width $\Delta \ln M \sim 0.3$ between the SDSS completeness limit in the respective redshift interval and $10^{15}\,h^{-1}M_\odot$. The total counts received from all clusters per mass bin drop much less steeply than the cluster number because the number of counts received per cluster increases strongly with cluster mass. The error bars bracket results obtained by changing σ_8 by ±0.1 and illustrate the sensitivity to the power-spectrum normalisation.

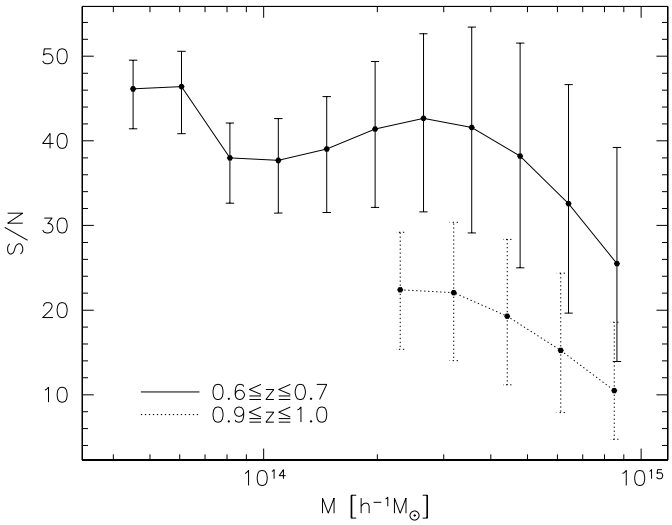

Fig. 8. Signal-to-noise ratios in stacked cluster fields in the given mass bins for the two redshift intervals $0.6 \le z \le 0.7$ (solid curve) and $0.9 \le z \le 1.0$ (dotted curve). As in Fig. 7, the error bars show the range obtained by varying σ_8 by ±0.1. The signal-to-noise ratio in the lower redshift interval reaches ∼40 near $3 \times 10^{14}\,h^{-1}M_\odot$. Even near $10^{15}\,h^{-1}M_\odot$ in the upper redshift interval, the signal-to-noise ratio is ∼10.

SDSS only covers a quarter of the sky. Figure 7 shows the resulting cluster numbers ΔN_{ij} and the total photon numbers ΔC_{ij} expected from these clusters. The solid and dotted curves show results for the lower and upper redshift bins, respectively. In order to illustrate the sensitivity of the results to σ_8, the error bars mark the range obtained for $\sigma_8 = 0.9 \pm 0.1$. The curves showing the total photon counts received in each mass bin are flatter than those showing the total cluster number because clusters with higher mass are more X-ray luminous.

The figure shows that, even with relatively fine mass binning, more than 10^4 clusters should be detectable per mass bin below $10^{14}\,h^{-1}M_\odot$ in the lower redshift interval $0.6 \le z \le 0.7$. For comparison, Fig. 6 shows that several hundred stacked cluster fields are already sufficient for a 5-σ X-ray detection in the RASS. Similarly, more than 10^3 clusters are expected per mass bin below $4 \times 10^{14}\,h^{-1}M_\odot$ at higher redshifts, $0.9 \le z \le 1.0$, where fewer than ∼100 cluster fields need to be stacked for an X-ray detection. A useful way to quantify these numbers is by calculating the expected signal-to-noise ratio in a stack of all the cluster fields in each mass bin and in each of our two redshift intervals. The results are shown in Fig. 8.

At the lower redshift the signal-to-noise ratio starts above 40 near $4 \times 10^{13}\,h^{-1}M_\odot$, where the contribution of metal lines to the flux is high. With increasing mass, the line contribution decreases and S/N has a shallow minimum near $10^{14}\,h^{-1}M_\odot$. Increasing continuum emission causes a broad peak at ≳40 centred on $3 \times 10^{14}\,h^{-1}M_\odot$. It then decreases slowly towards higher masses. The drop-off results from from the low cluster number at the high-mass end. If we set the metal abundance to zero, the low X-ray flux at the low-mass end makes the signal-to-noise drop to ∼20 near $4 \times 10^{13}\,h^{-1}M_\odot$. Even in the upper redshift interval, the signal-to-noise ratio is above 10, rising to ≳20 in the lowest mass bin. These results are, however, very sensitive to σ_8. Near $10^{15}\,h^{-1}M_\odot$ in the upper redshift interval, the signal-to-noise ratio varies between ∼5 and ∼20 as σ_8 is increased from 0.8 to 1.0.

The high signal-to-noise ratio even for high-redshift clusters encourages us to investigate whether it will be possible to estimate cluster temperatures from hardness ratios. We introduce two energy bands, one with $0.5 \le E/\mathrm{keV} < 1$ and the second with $1 \le E/\mathrm{keV} \le 2$. The counts $C_{1,2}$ in these two bands determine the hardness ratio

$$\mathcal{R} = \frac{\text{hard counts}}{\text{soft counts}} = \frac{C_2}{C_1}. \tag{22}$$

We use *xspec* to compute the hardness ratio $\mathcal{R}(T,z)$ expected for RASS data for clusters with temperature T at redshift z. For clusters of mass M at redshift z, the uncertainty in the temperature measurement is then

$$\Delta T(M,z) = \left(\frac{\partial \mathcal{R}}{\partial T}[T(M),z]\right)^{-1} \Delta\mathcal{R}, \tag{23}$$

where the uncertainty $\Delta\mathcal{R}$ of the measured hardness ratio (22) is determined by the count statistics. The boundaries of the energy bands were chosen so that $\mathcal{R}$ is typically of order unity in the mass and redshift ranges considered here. The signal-to-noise ratio of the hardness ratio $\mathcal{R}/\Delta\mathcal{R}$ is ≳10 for all cluster mass bins in the redshift interval $0.6 \le z \le 0.7$, and is ≳8 for the bins in the redshift interval $0.9 \le z \le 1.0$. The derivative of $\mathcal{R}$ with respect to T is ∼0.8 for $T \sim 1$ keV and falls to ∼0.1 for the highest temperatures. As a result temperature determinations should be most accurate for clusters with $M \sim 10^{14}\,h^{-1}M_\odot$; at lower masses, line emission in the low-energy band dominates and the uncertainty $\Delta\mathcal{R}$ increases because of poor photon statistics in the high-energy band. We show T and $\Delta T/T$ in Fig. 9 for

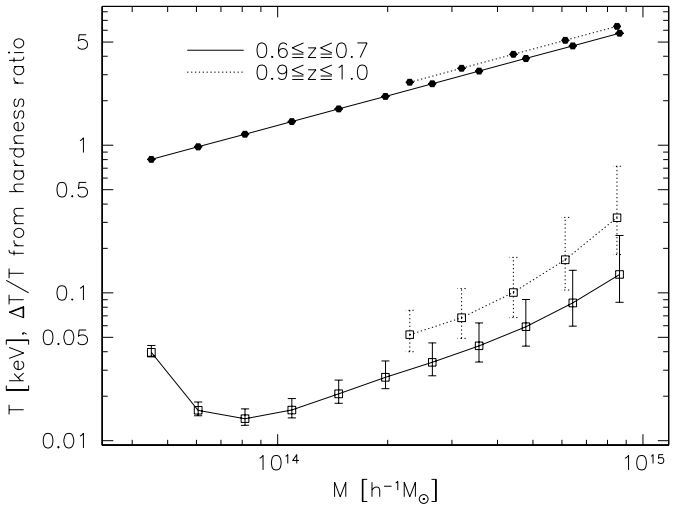

Fig. 9. The curves with open squares show the relative uncertainty $\Delta T/T$ of cluster temperatures determined from the hardness ratio between a soft ($E \in [0.5, 1]$ keV) and a hard ($E \in [1, 2]$ keV) band. Clusters are stacked in mass bins in the two redshift intervals $0.6 \leq z \leq 0.7$ (solid curve) and $0.9 \leq z \leq 1.0$ (dotted curve). As in Figs. 7 and 8, the error bars indicate the range obtained by varying σ_8 by ± 0.1. The temperature uncertainty reaches a minimum of $\lesssim 2\%$ near $8 \times 10^{13}\, h^{-1}\, M_\odot$ and falls below 10% except for the highest-mass bin in the lower redshift interval. Even for massive clusters at high redshift, the temperature uncertainty is expected to be $\lesssim 50\%$. The curves with filled circles show the cluster temperature in keV for the given mass bins and redshift intervals.

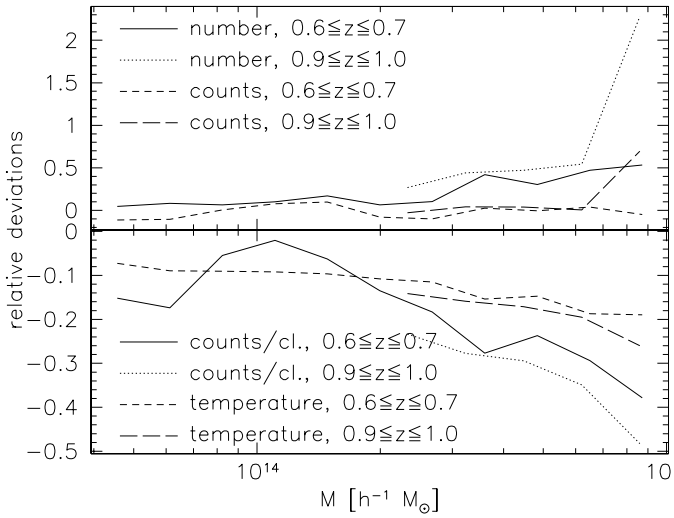

Fig. 10. Relative deviations of various cluster population properties from theoretical expectations, caused by the scatter in the relations between cluster mass and cluster richness or X-ray luminosity. Clusters are binned according to the mass inferred from their optical richness. Due to the steeply decreasing underlying cluster mass function, the uncertainty in inferred mass scatters on average more clusters from lower to higher masses than the reverse. The clusters sorted into a given mass bin according to optical richness are thus typically somewhat less massive than the bin. Hence the cluster numbers as functions of mass are typically overestimated. For the same reason, the temperature in a given mass bin tends to be biased low.

the same mass bins and redshift intervals used previously. For comparison, the plot also gives the mean cluster temperature expected as a function of mass in each redshift interval. Note that T is the emitted rather than the observed value.

Figure 9 shows that the relative uncertainty in the mean temperature of the clusters in each mass bin is remarkably small for $0.6 \leq z \leq 0.7$. Except for the highest-mass bin, it is $\lesssim 10\%$ and reaches a minimum of $\lesssim 2\%$ at $M \approx 8 \times 10^{14}\, h^{-1}\, M_\odot$. Over the mass range 10^{14}–$10^{15}\, h^{-1} M_\odot$, it appears that a $>10\,\sigma$ measurement of cluster temperature should be possible. As in Figs. 7 and 8, the error bars in Fig. 9 indicate the range obtained by varying the power-spectrum normalisation σ_8 by ± 0.1. For clusters in the high-redshift band, $0.9 \leq z \leq 1.0$, the relative temperature uncertainty increases both because of count statistics and because of decreasing sensitivity of $\mathcal{R}$ to T. Despite this, temperature measurements at 5 to $10\,\sigma$ should be possible. Note that a careful maximum likelihood measurement of T would give results with somewhat higher significance than the simple hardness ratio approach we have adopted here.

5. Optical mass estimates; biases

So far, we have binned clusters by mass, which is impossible with real cluster samples. In practice, masses will have to be estimated from observable quantities. Since the clusters in the proposed study will be optically selected and stacked to obtain their average X-ray properties, mass estimates based on optical properties have to be used. In a recent paper, Yee & Ellingson (2003) investigated the cross correlation between dynamical mass estimates and optical richness of clusters in the CNOC1 cluster redshift survey. They used the galaxy-cluster centre correlation amplitude, $B_{\rm cg}$, as a measure for optical cluster richness (cf. Longair & Seldner 1978; Yee & López-Cruz 1999). They find

$$\log\left(\frac{M_{200}}{h_{50}^{-1}\, M_\odot}\right) = (0.47 \pm 0.16)\, \log B_{\rm cg} + (10.05 \mp 0.89). \quad (24)$$

We investigate the scatter introduced into our results by binning clusters according to richness $B_{\rm cg}$ instead of mass. We create random cluster samples in the two redshift intervals $0.6 \leq z \leq 0.7$ and $0.9 \leq z \leq 1.0$, following the distribution (1) in mass and redshift. Fitting the data by Yee & Ellingson (2003), we invert (24) and assign to each cluster of mass M_{200} an optical richness $B_{\rm cg}$ with a relative Gaussian scatter of 22% estimated from the data. Likewise, we use (4) for assigning an X-ray luminosity to clusters of mass M and apply a relative Gaussian scatter of 45% estimated from the data given by Reiprich & Böhringer (2002). For all randomly drawn clusters, we thus obtain X-ray counts in the soft and hard bands defined above, and a richness parameter $B_{\rm cg}$. We then estimate their mass using (24) and bin them into the same mass bins as defined above. Thus, this procedure mimics binning clusters according to optically determined mass estimates rather than their true mass. We checked that the analytic results described in the earlier sections are accurately reproduced by this Monte-Carlo approach. Figure 10 summarises results for the relative deviations of various cluster population properties from the theoretical expectations.

The uncertainty in the cluster mass derived from optical richness scatters low-mass clusters into higher-mass bins and vice versa. Since the mass function falls steeply, more low-mass clusters are moved towards higher mass than the reverse. The cluster number in particular in the highest mass bins thus tends to be overestimated. The solid and dotted curves in the upper panel of Fig. 10 show that this bias can reach 40%–50% for clusters at redshift $0.6 \le z \le 0.7$ with masses near $10^{15}\,h^{-1}\,M_\odot$, and more for clusters in the higher-redshift interval. Two effects compete for the X-ray counts received. The cluster number per bin increases, but their X-ray flux is lower because of their lower mass and temperature. The short- and long-dashed curves in the upper panel of Fig. 10 show that the X-ray counts are less affected than the cluster number, but tend to be biased low.

The solid and dotted curves in the lower panel of Fig. 10 illustrate that the counts received per cluster are consequently underestimated by typically 10%–20% at intermediate masses, and by 20%–40% at higher masses. The preferential contamination by low-mass clusters also causes cluster temperatures to be underestimated by typically 10%–20% (short- and long-dashed curves).

Biases due to the considerable scatter in the relation between mass and X-ray luminosity (cf. Fig. 1) are virtually irrelevant because of the large number of clusters per mass bin. On the whole, the biases due to mass estimates derived from optical richness are moderate. Since they depend on the shape of the mass function and the scatter in the relation between estimators of optical richness and cluster mass, they can be quantified and removed. This procedure might have to be performed iteratively because the assumed underlying mass function must consistently be adapted to the cluster number and X-ray counts observed. It should be noted, however, that it is as yet unclear how reliable cluster mass determinations based on optical richness will be if applied to cluster catalogues obtained from the SDSS using Dalcanton's (1996) surface-brightness enhancement technique. The actual relation between mass and optical richness may thus differ from Yee & Ellingson's (2003) relation (24).

6. Discussion

Ongoing and planned wide-area surveys will detect tens of thousands of galaxy clusters out to redshifts near and above unity. For example, searching for surface-brightness enhancements in a smoothed stack of the r'-, i'- and z'-band data of the Sloan Digital Sky Survey should allow clusters of $5 \times 10^{13}\,h^{-1}M_\odot$ to be detected out to $z \sim 0.7$, while $z > 1$ is reached for masses above $\sim 3{\times}10^{14}\,h^{-1}M_\odot$ (Bartelmann & White 2002).

We have investigated here whether existing X-ray data can be used to measure the X-ray emission of these clusters by stacking sufficiently many fields. We assume clusters to be distributed in mass and redshift as given by the numerical results of Jenkins et al. (2001). Their temperatures are taken to be proportional to $[M\,h(z)]^{2/3}$, with the normalisation taken from the N-body/SPH simulations of Mathiesen & Evrard (1901). We adopt the observed low-redshift relation between bolometric X-ray luminosity and temperature, and we assume that it holds at all redshifts. Although the temperature-mass and luminosity-temperature relations are subject of debate, they imply a relation between X-ray luminosity and mass which agrees excellently with observational results from Reiprich & Böhringer (2002; cf. Fig. 1). We model cluster X-ray surface-brightness profiles by a beta profile, although this has little effect on our results because most distant clusters are not resolved in the RASS. We convert the bolometric X-ray luminosity into a count rate using the *xspec* software, assuming a Raymond-Smith plasma model with a metallicity of 0.3 solar and a foreground neutral-hydrogen column of $4 \times 10^{20}\,\mathrm{cm}^{-2}$.

The only suitable survey of the X-ray sky is the ROSAT All-Sky Survey (RASS). With its median exposure time of approximately 415 s and its effective detector area of $\sim 230\,\mathrm{cm}^2$, it detected ~10 photons from a cluster of mass $10^{14}\,h^{-1}M_\odot$ at $z \sim 0.1$, and only about one photon from a similar cluster at $z \sim 0.5$. Since the effective angular resolution of the RASS is $\sim 2'$, cluster emission is typically spread over an effective solid angle of ~14 square arcminutes. Due to the low background of the PSPC detector, only ~1.5 background photons are expected within this solid angle during the median RASS exposure time. This corresponds to the number of photons expected from a cluster with mass $M \sim 10^{14}\,h^{-1}M_\odot$ at redshift $z \sim 0.35$, or with mass $M \sim 4 \times 10^{14}\,h^{-1}M_\odot$ at $z \sim 1$. Thus stacked cluster fields are background dominated at lower mass or higher redshift than this.

Requiring a signal-to-noise exceeding 5, we find that 100 fields must be stacked to get a significant detection of clusters with $M \sim 10^{14}\,h^{-1}M_\odot$ at $z \sim 0.4$, or with $M \sim 3 \times 10^{14}\,h^{-1}M_\odot$ at $z \sim 1.0$. A stack of ten cluster fields should give a 5-σ detection of massive clusters with $M \sim 10^{15}\,h^{-1}M_\odot$ at $z \sim 1.1$, should any such exist.

The number of clusters expected in wide-field surveys like the SDSS is enormous and allows the detection of X-ray emission from even fairly low-mass clusters out to surprisingly high redshift. In the redshift interval between 0.6 and 0.7, the surface-brightness technique of Dalcanton (1996) should detect clusters in the SDSS data down to a mass limit of $\sim 3.9 \times 10^{13}\,h^{-1}M_\odot$. If we bin the clusters by mass into logarithmic bins with width $\Delta \ln M = 0.3$, the signal-to-noise ratio for the X-ray detection exceeds 35 near $10^{14}\,h^{-1}M_\odot$, rises above 40 near $3 \times 10^{14}\,h^{-1}M_\odot$ and drops to ~25 at $10^{15}\,h^{-1}M_\odot$. In the interval between redshifts 0.9 and 1.0, the mass completeness limit for SDSS cluster detection increases to $2 \times 10^{14}\,h^{-1}M_\odot$, but X-ray detections are still possible with signal-to-noise ratios above 10 if clusters are binned by mass as described.

We have also shown that the signal-to-noise ratio of the stacked cluster images is high enough to divide the photons into two energy bands, $E \in [0.5, 1]$ and $E \in [1, 2]$, and to estimate cluster temperatures from the count ratio. In particular, for clusters with $0.6 \le z \le 0.7$ and masses near $10^{14}\,h^{-1}M_\odot$, the hardness ratio changes with cluster temperature sufficiently strongly for mean cluster temperatures to be determined with a typical relative uncertainty of $\Delta T/T \lesssim 2\%$.

Of course, these results depend on the modelling assumptions we have made. Their sensitivity to changes in the power-spectrum normalisation σ_8 is shown in Figs. 7–9, where the error bars bracket results obtained adopting $\sigma_8 = 0.9 \pm 0.1$.

Other critical assumptions are that the relation between bolometric X-ray luminosity and temperature is independent of redshift, and that the cluster temperature scales with cluster mass as given by simulations. Our assumptions about cluster X-ray profiles are less critical because of the low angular resolution of the RASS.

Using photometric redshifts for brightest cluster members, it should be possible to determine redshifts for SDSS clusters with an accuracy of $\Delta z \sim 0.05$. On the other hand, rather rough estimates of cluster mass can be obtained from the optical data. Following the result by Yee & Ellingson (2003) that the correlation between cluster mass and a quantitative measure for optical richness, the galaxy-cluster centre correlation amplitude $B_{\rm cg}$, is reasonably tight, we have performed a Monte-Carlo experiment to quantify possible biases resulting from the scatter in optical mass estimates. The main effect is that the steeply falling mass function causes more low-mass clusters to be scattered into higher-mass bins than the reverse, causing a contamination of high-mass bins by lower-mass clusters. Cluster numbers per mass bin thus tend to be overestimated, while the X-ray counts per cluster and the cluster temperatures tend to be underestimated. The biases are, however, relatively moderate and are typically $\lesssim$20%−30% for the counts per cluster, and $\lesssim$20% for the cluster temperature. In addition, the magnitudes of these biases can be estimated from the assumed shape of the cluster mass function and the scatter in the optical mass estimator, and can thus be removed. This procedure may have to be performed iteratively to achieve consistency between the cluster mass function and the X-ray counts. The optically selected clusters in a given redshift interval can also be binned by magnitude, and the study suggested here will then give relations between optical luminosity and mean X-ray luminosity and temperature.

Wide-area surveys in the microwave regime will be carried out in the near future which will detect of order one cluster per square degree trough the thermal Sunyaev-Zel'dovich effect. The *Planck* satellite, for instance, due for launch in early 2007, is expected to detect of order 30 000 galaxy clusters on the sky outside the Galactic plane, approximately 10% of which will be at redshifts beyond 0.5. Stacking these clusters in the same way as described here, and combining their total integrated Compton-y parameter with their X-ray emission, will allow their total baryonic mass and perhaps their temperatures to be constrained.

Acknowledgements. We thank the anonymous referee for comments which strengthened our results.

References

Allen, S. W., & Fabian, A. C. 1998, MNRAS, 297, L57
Arnaud, K. A. 1996, ADASS 5, 17, ed. G. H. Jacoby & J. Barnes
Bardeen, J. M., Bond, J. R., Kaiser, N., & Szalay, A. S. 1986, ApJ, 304, 15
Bartelmann, M. & White, S. D. M. 2002, A&A, 388, 732
Carroll, S. M., Press, W. H., & Turner, E. L. 1992, ARA&A, 30, 499
Cavaliere, A., & Fusco-Femiano, R. 1978, A&A, 70, 677
Dalcanton, J. J. 1996, ApJ, 466, 92
Dickey, J. M., & Lockman, F. J. 1990, ARA&A, 28, 215
Ebeling, H., Edge, A. C., & Henry, J. P. 2001, ApJ, 553, 668
Eke, V. R., Cole, S., & Frenk, C. S. 1996, MNRAS, 282, 263
Evrard, A. E., MacFarland, T. J., Couchman, H. M. P., Colberg, J. M., et al. 2002, ApJ, 573, 7
Fukazawa, Y., Makishima, K., Tamura, et al. 1998, PASJ, 50, 187
Gonzalez, A. H., Zaritsky, D., Dalcanton, J. J., & Nelson, A. 2001, ApJS, 137, 117
Hashimoto, Y., Hasinger, G., Arnaud, M., Rosati, P., & Miyaji, T. 2002, A&A, 381, 841
Hasinger, G., Boese, G., Predehl, P., et al. 1995, MPE/OGIP Calibration Memo CAL/ROS/93-015
Henry, J. P. 2003, in Matter and Energy in Clusters of Galaxies, ed. C.-Y. Hwang & S. Bowyer, in press
Ikebe, Y., Reiprich, T. H., Böhringer, H., Tanaka, Y., & Kitayama, T. 2002, A&A, 383, 773
Jenkins, A., Frenk, C. S., White, S. D. M., et al. 2001, MNRAS, 321, 372
Jones, L. R., Scharf, C., Ebeling, H., et al. 1998, ApJ, 495, 100
Lahav, O., Bridle, S. T., Percival, W. J., Peacock, J. A., et al. 2002, MNRAS, 333, 961
Łokas, E. L., & Hoffman, Y. 2001, preprint [astro-ph/0108283]
Longair, M. S., & Seldner, M. 1979, MNRAS, 189, 433
Mathiesen, B. F., & Evrard, A. E. 2001, ApJ, 546, 100
Mohr, J. J., Mathiesen, B., & Evrard, A. E. 1999, ApJ, 517, 627
Mushotzky, R. F., & Scharf, C. A. 1997, ApJ, 482, L13
Navarro, J. F., Frenk, C. S., & White, S. D. M. 1995, MNRAS, 275, 720
Nevalainen, J., Kaastra, J., Parmar, A. N., et al. 2001, A&A, 369, 459
Pierpaoli, E., Scott, D., & White, M. 2001, MNRAS, 325, 77
Press, W. H., & Schechter, P. 1974, ApJ, 187, 425
Reichart, D. E., Castander, F. J., & Nichol, R. C. 1999, ApJ, 516, 1
Reiprich, T. H., & Böhringer, H. 2002, ApJ, 567, 716
Snowden, S. L., & Schmitt, J. H. M. M. 1990, Ap&SS, 171, 207
Raymond, J. C., & Smith, B. W. 1977, ApJS, 35, 419
Rosati, P., Borgani, S., & Norman, C. 2002, ARA&A, 40, 539
Schindler, S. 1999, A&A, 349, 435
Sheth, R. K., & Tormen, G. 2002, MNRAS, 329, 61
Sheth, R. K., Mo, H. J., & Tormen, G. 2001, MNRAS, 323, 1
Snowden, S. L., Freyberg, M. J., & Plucinsky, P. P., et al. 1995, ApJ, 454, 643
Viana, P. T. P., & Liddle, A. R. 1996, MNRAS, 281, 323
Viana, P. T. P., Nichol, R. C., & Liddle, A. R. 2002, ApJ, 569, L75
Vikhlinin, A., McNamara, B. R., Forman, W., et al. 1998, ApJ, 498, L21
Vikhlinin, A., Van Speybroeck, L., Markevitch, M., Forman, W. R., & Grego, L. 2002, ApJ, 578, L107
White, S. D. M., Efstathiou, G., & Frenk, C. S. 1993, MNRAS, 262, 1023
Yee, H. K. C., & López-Cruz, O. 1999, AJ, 117, 1985
Yee, H. K. C., & Ellingson, E. 2003, ApJ, 585, 215
Zaritsky, D., Shectman, S. A., & Bredthauer, G. 1996, PASP, 104, 108